The International Journal of Advanced Manufacturing Technology (2024) 132:1883–1895
https://doi.org/10.1007/s00170-024-13484-0

ORIGINAL ARTICLE

Structure and mechanical properties of three-layer composites obtained by magnetic pulse welding of titanium and Zr-based metallic glass

Daria V. Lazurenko[1,2] · Alexander A. Ivannikov[3] · Alexander G. Anisimov[4] · Nikita S. Popov[3] · Kemal I. Emurlaev[1,5] · Gleb D. Dovzhenko[1,5] · Ivan A. Bataev[1] · Ruslan I. Kuzmin[1] · Konstantin E. Kuper[5,6]

Received: 7 November 2023 / Accepted: 19 March 2024 / Published online: 25 March 2024

Abstract
Metallic glass-reinforced metal matrix composites (MMCs) are in the focus of attention of many research groups due to the outstanding properties provided by a combination of ductile crystalline matrix and high-strength glassy phase. To date, many fabrication techniques have been used to form such composites. Most of them are based on pressure-assisted sintering of glassy and crystalline components. However, the selection of the heating temperature and holding time is challenging due to the low thermal stability of the metallic glasses (MGs). In this study, a solid-state magnetic pulse welding (MPW) technique was used for manufacturing laminated Ti-based composites with Zr-based MG reinforcement. The structure of the interfaces between Ti and MG layers was studied using light microscopy (LM), scanning electron microscopy (SEM), and synchrotron X-ray diffraction (SXRD). The experimental study was supplemented with smoothed-particle hydrodynamics (SPH) numerical simulations. The Ti-MG-Ti composite obtained by MPW possessed high quality of joint and had no macroscopic defects such as cracks or lack of fusion. The formation of a firm joint was provided by the plastic flow of titanium. Deformation processes in the titanium plates developed mainly in the interfacial zones, while the MG ribbons subjected to deformation by shear mechanism through the entire thickness. Due to the short-term thermal impact and high cooling rates, MPW retained a disordered structure of MG, despite local melting occurring at the interfaces and in shear bands. Tensile tests of composites containing 5 vol. % and 13 vol. % of MG phase showed that their strength follows the rule of mixtures.

Keywords Metallic glass · Metal matrix composites · Laminated composites · Magnetic pulsed welding · Numerical simulation

✉ Daria V. Lazurenko
pavlyukova_87@mail.ru

[1] Novosibirsk State Technical University, Karl Marks Av. 20, 630073 Novosibirsk, Russia

[2] St Petersburg State University, Universitetskaya Embankment, 7-9, 199034 St Petersburg, Russia

[3] National Research Nuclear University MEPhI (Moscow Engineering Physics Institute), Kashirskoye Shosse, 31, 115409 Moscow, Russia

[4] Lavrentiev Institute of Hydrodynamics SB RAS, Lavrentiev Av., 15, 630090 Novosibirsk, Russia

[5] Synchrotron Radiation Facility - Siberian Circular Photon Source (SKIF), Boreskov Institute of Catalysis SB RAS, Kol'tsovo 630559, Russia

[6] Budker Institute of Nuclear Physics of Siberian Branch, Russian Academy of Sciences, Lavrentiev Av. 11, 630090 Novosibirsk, Russia

1 Introduction

Although metallic glasses (MGs) have been known for a long time, their use as load-bearing materials is still limited. Possessing high hardness, strength, and wear resistance, MGs have limited ductility when deformed [1–3]. For this reason, their use as a reinforcing component in metal matrix composites (MMCs) seems to be more promising [4]. Higher strength and toughness can be achieved by combining the properties of ductile crystalline matrix and strong reinforcing phase of an amorphous nature. This approach has been successfully used in a number of investigations and has been tested for a variety of combinations of amorphous alloys and metal matrices, as it was shown in a recent review of Georgarakis et al. [5]. The amorphous phase can be introduced into the metal matrix in the form of ribbons and their fragments [6–8], as powders [9, 10]

or as fibers [11]. The advantages of the first approach are due to the possibility of forming material with improved transverse properties, while in materials reinforced by particles or fibers, MG inclusions serve as obstacles to the movement of dislocations in the matrix. Furthermore, the hardening effect is observed when implementing any approach [7, 10].

Most currently used methods for the production of MG-reinforced MMCs are based on co-heating of the composites' components. These methods include but not limited to sintering with pre-pressing [12], hot pressing [6, 13–15] and spark plasma sintering [16–18]. To form the ribbon-reinforced MMCs, techniques such as warm rolling [8] or infiltration casting [7] can be applied. However, the methods involving thermal exposure are associated with a number of difficulties. Due to their metastable nature, MGs have low thermal stability and crystallize even when heated to fairly low temperatures [3]. Crystallization of the glassy phase during the production of a composite can significantly deteriorate its properties [18]. Therefore, the fabrication regimes of composites should be carefully controlled to avoid partial or complete crystallization of MG [14, 19].

A promising approach to form MG-reinforced MMCs without significant thermal effects is high-velocity impact welding, such as explosion welding (EW) or magnetic pulse welding (MPW). As opposite to other welding or cladding methods [20–25], EW and MPW are the solid state processes which do not induce bulk melting of the materials. Both methods are based on the principle of high-velocity oblique impact of welded workpieces [8]. It is believed that upon the impact, a jet is formed between the workpieces, which cleans the surfaces of oxides and contaminants. High impact pressures improve the ability of metals to deform plastically within a short period of time. Thus, due to the action of very high pressures, the clean surfaces come into close contact with each other and form strong metallurgical bond, while simultaneously undergoing shear deformation. During welding, only a thin layer of the workpieces is subjected to heating. In this way, it is possible to preserve the disordered state of MG, which was shown in studies devoted to the joining of crystalline metals and MGs by EW [26–31]. Due to high cooling rates, local heating at the interfaces does not induce the crystallization of the amorphous alloy [32].

The possibility of using MPW to join amorphous and crystalline alloys was already demonstrated in our previous studies [33, 34]. However, a number of phenomena, such as saturation of mixing zones with nitrogen and local through melting of the amorphous ribbon during the welding remained unexplained. For this reason, in the present work, a comprehensive study of the joint formation was carried out, which was based on experiments and numerical simulation of the welding process. The features of the composite interfaces obtained under different impact velocities were analyzed and the influence of the amorphous phase fraction on the strength of the composite was assessed.

2 Materials and methods

2.1 Materials and methods of the experimental investigations

Commercially pure (cp) Ti foils (99.33 Ti; 0.25 Fe; 0.07 C; 0.1 Si; 0.04 N; 0.2 O; 0.01 H, all wt. %) with a thickness of 500 µm and Zr-based MG ribbons (35Zr-25Ti-28Be-12Cu, all at. %) with thicknesses of 50 and 150 µm were used as starting materials. The width and the length of the workpieces for welding were 20 mm and 150 mm, respectively.

The MG ribbons were produced by melt spinning in the helium atmosphere using a Kristall-702 apparatus [35]. The melt was cooled on a copper disk rotating at a linear speed of 20 m/s, providing a cooling rate in the range of 10^4–10^6 K/s. The as-spun ribbons possessed fully amorphous structure (Fig. 1). The crystallization and glass transition temperatures were found from differential scanning calorimetry (DSC) curves. According to Fig. 2, the MG crystallizes between 445 and 477 °C, the glass transition temperature is ranging from 299 to 357 °C. The melting temperature is 712 °C.

MPW was performed at the Lavrentiev Institute of Hydrodynamics (Novosibirsk, Russia) [36]. A capacitor battery with capacitance of 3.4×10^{-3} F and voltage of 5 kV was used as a power source. The battery accumulated up to 40 kJ of energy. The total inductance of the battery and input cables was within 40 nH. The battery discharge was initiated using a solid-state discharger. The discharge current in the experiment was recorded by an inductive sensor. The magnetic pressure, the travel distance and the velocity of the driver plate were found from the dependence of the square of the current on time. These values, together with the distance between the driven plate and the target, made it possible to set the impact velocity.

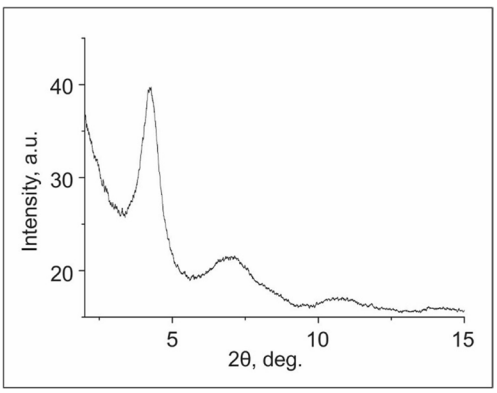

Fig. 1 SXRD pattern of rapidly solidified Zr-based alloy

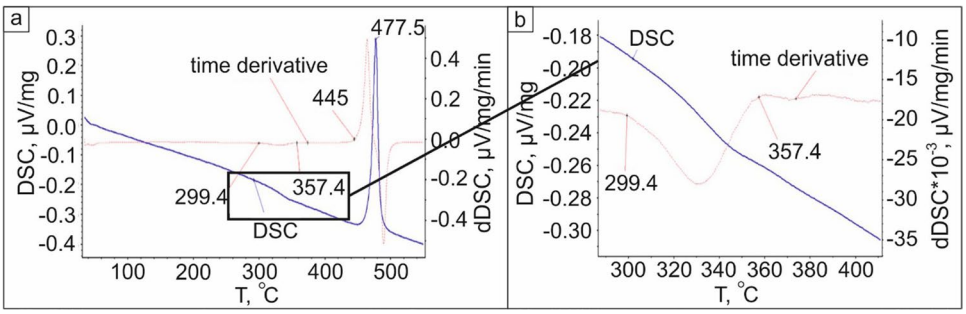

Fig. 2 DSC curves obtained from rapidly solidified Zr-based MG (**a**) and the magnified image of the area marked with rectangle in a (**b**)

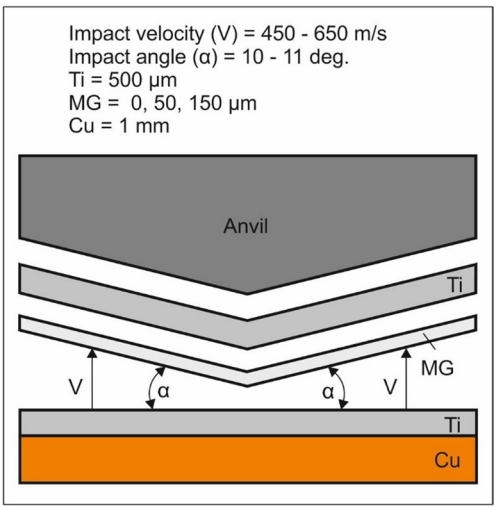

Fig. 3 Scheme of the plate arrangement for MPW

A copper plate with a thickness of 1 mm and a width of 30 mm was used as a driver plate, which was necessary to accelerate Ti and MG foils. The driver plate was not welded to the composite. The arrangement of the plates is shown in Fig. 3. The upper titanium plate was accelerated by the copper driver plate. Next, they collided first with the MG ribbon, and then with the lower titanium plate. The collision angle equal to 10° was ensured by a V-shaped anvil. This particular angle value was chosen from a series of preliminary experiments. By calculations, it was found that at the initial stages of welding, the flyer plate collided with the target at a velocity of 450 m/s, and then at the end of welding the velocity increased to 650 m/s.

The structure of the as-welded composite was studied by light microscopy (LM) in the differential interference contrast using a Carl Zeiss Axio Observer Z1m microscope and scanning electron microscopy (SEM) in the backscattered electrons mode using a Carl Zeiss EVO 50 microscope equipped with an Oxford Instruments X-Act energy-dispersive X-ray (EDX) detector. The samples for microscopic studies were prepared by grinding with sandpapers (P120–P2500) and alumina powder with a particle size of 5 and 1 μm, followed by polishing with colloidal silica.

Synchrotron X-ray diffraction (SXRD) experiment was carried out at Siberian Center for Synchrotron and Terahertz Radiation on an 8-A beamline of the VEPP-4 accelerating-storage complex (Budker Institute of Nuclear Physics SB RAS, Novosibirsk, Russia). The studies were carried out in transmission geometry using monochromatic radiation with the wavelength of 0.178 Å. The sample-to-detector distance was 509 mm. A beam size was 200 × 200 μm^2. SXRD patterns were recorded using a Mar345s 2D detector with a resolution of 3500 × 3500 pixels and a pixel size of 200 × 200 μm^2. The azimuthal integration was performed using the self-developed code based on PyFAI open-source module in the Python programming language [37]. CeO_2 was used as a calibrant.

The Martens hardness and elastic modulus were measured on a FSBI TISNCM NanoScan 4D device by indenting a diamond pyramid with a load of 1 N. The tensile strength of the samples was measured using an Instron 3369 testing machine. The load was applied along the layers. The samples were prepared by wire discharge machining. The sample dimensions were 30 × 10 × 1.05 mm and 30 × 10 × 1.15 mm, respectively, for the composites with 50 μm and 150 μm MG ribbons. A sample obtained by MPW of two titanium plates was used for the purpose of comparison.

2.2 Simulation of the MPW process

The collision of two titanium foils and an amorphous ribbon located between them was simulated by smoothed-particle hydrodynamics (SPH) method using Ansys Autodyn software. The simulation was performed in 3D formulation. The particle size was 0.005 mm. The initial location and size of the plates are shown in Fig. 4. The simulations were carried out for impact velocities of 450, 550, and 650 m/s and a collision angle of 10°.

The modified Mie-Grüneisen equation of state (which is called Shock in terms of the Ansys Autodyn software) was used to model titanium at high pressures (Table 1). The yield stress of titanium was calculated using the Johnson–Cook (JC) model, which takes into account the effects of strain hardening and thermal softening and is suitable for the metallic materials under high-velocity impact

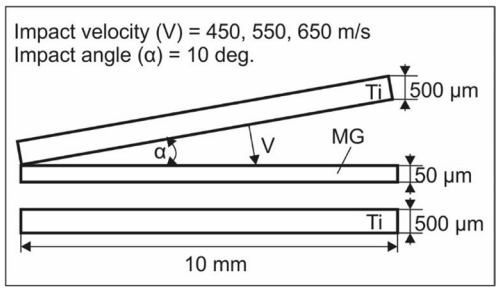

Fig. 4 The scheme of the simulation domain

Table 1 The Mie-Grüneisen equation of state parameters for cp-Ti [38]

Initial density, ρ_0 (kg/cm^3)	Gruneisen coefficient, Γ_0	Coefficient C_1 (m/s)	Coefficient S_1	Initial temperature (K)	Specific heat (J/kg·K)
4510	1.23	5130	1.28	300	523

conditions. The material constants were taken from the study of Nassiri et al. [38] (Table 2).

The properties of MGs differ significantly from the properties of ductile polycrystalline materials. Possessing no crystalline structure, MGs are not able to deform by slip of dislocations or mechanical twinning. In studies [28, 39], the Johnson-Holmquist II (JH-2) model was proposed to estimate the mechanical response of MGs at high strain rates. The constants for JH-2 model of Zr-based MG were found in [39] (Table 3). The equation of state for MG was described by polynomials [28].

3 Results

3.1 Characterization of the structure and results of numerical simulations

Microscopic analysis of the samples obtained by MPW revealed a good quality of the interfaces (Fig. 5). At both lower and upper boundaries between titanium and the amorphous alloy, no unwelded spots were observed along the entire length of the welds. The upper interface was more tortuous, with an aperiodic wave-like morphology. The titanium located near the interface experienced severe plastic deformation. The plastic flow was uneven, as evidenced by the presence of severely deformed zones with elongated titanium grains (indicated by a yellow dotted line in Fig. 5a) adjacent to less deformed areas characterized by presence of deformation twins inside virtually undeformed grains.

With an increase of impact velocity, the thickness of the deformed layers increased (Fig. 6a, b). In the lower titanium plate the thickness of the deformed layer was smaller than in the upper one, which is explained by a decrease in the velocity during the second collision compared to the first one [40]. A decrease in collision velocity and, accordingly, dissipated energy leads to a decrease in plastic deformation.

The numerical simulation confirms this assumption. From Fig. 7 one may conclude, that when the impact velocity increases, the thickness of the deformed layer also increases. The materials near the first interface experience additional deformation when two upper plates collide with the lower one, which is clearly seen in Fig. 7b, c. The trend of increasing the thickness of the deformed layer with increasing the impact velocity was clearly reproduced in numerical

Table 2 The JC model parameters for cp-Ti [38]

Shear modulus, G (GPa)	Yield stress, A (MPa)	Strain hardening modulus, B (MPa)	Strain hardening exponent, n	Strain-rate dependence coefficient, c	Softening exponent, m	Melting temperature, T_{melt} (K)
41.1	359	668	0.49	0.0194	0.5816	1938

Table 3 The JH-2 model parameters for Zr-based MG [39]

Density, ρ (g/cm3)	Bulk modulus, K1 (GPa)	Shear modulus, G (GPa)	Elastic modulus, E (GPa)	Poisson's ratio, ν	Hugoniot elastic limit, HEL (GPa)	Maximum tensile strength, T (GPa)	Intact strength coefficient, A	Intact strength exponent, N
6.56	110.50	31.45	86.19	0.37	6.41	1.128	1.21	0.49
Strain rate coefficient, C	Fractured strength coefficient, B	Fractured strength exponent, M	Damage coefficient, D1	Damage coefficient, D2	Pressure coefficient 2, K2 (GPa)	Pressure coefficient 3, K3 (GPa)	Bulk factor, β	Maximum normalized fracture strength, σ^x_{fmax}
−0.0224	0.94	0.58	0.003	2.85	208.4	359.3	1.0	1.0

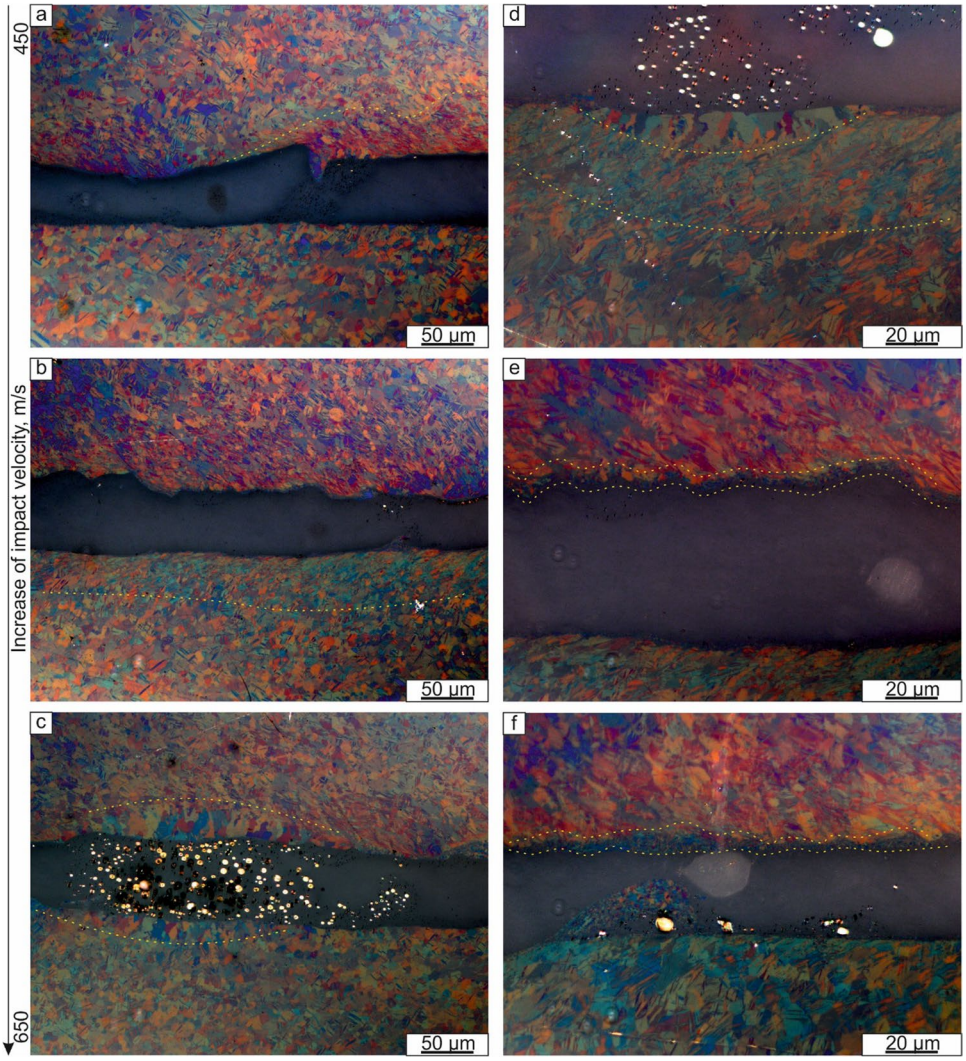

Fig. 5 LM micrographs obtained in differential interference contrast: the impact velocity increases from a to c and from d to f. Yellow dotted lines denote deformed layers and recrystallized grains in titanium

simulation, as can be seen in Fig. 6c, d. Based on the performed analysis, one can conclude on a good agreement between the experimental results and the simulation. However, the thickness of the deformed layers in the experimental sample was slightly lower than that predicted by model. Most likely, this is due to the inaccuracy of measurements performed by LM. Firstly, as noted above, the deformation was distributed unevenly, and, secondly, the metallographic analysis took into account only the thickness of the most severely deformed layer, although in fact slight traces of deformation were observed over almost the entire cross section of the titanium plates. For this reason, accurate experimental assessment of the thickness of deformed layers in titanium has proven difficult. Another reason for the differences between experimental and simulation results can be related to the model assumptions. First, the exact composition of MG used during the simulation was slightly different from that in the experiment. Even though the properties of Zr-based MG are quite similar [41, 42], the discrepancy could influence the result. Second, the model does not take into account the influence of the Ti alloy microstructure on its properties, as well as the effects related to possible solid-state phase transformations. Thus, any structural dependent particularities of the material behavior are missed. Also, the temperature dependent behavior of MG (e.g., superplastic behavior of MG near the glass transition temperature) was not included to the model. And third, the influence of environment was not considered, for instance, the effect of shock-compressed gas in the gap between the plates was neglected.

The other peculiarity of the structure near the interfaces was the appearance of recrystallized grains in titanium. Formation of thin recrystallized layers occurred already at medium velocities (Fig. 5b, e). As the impact velocity increased, the layer thickness increased from approximately 3 to 17 μm (indicated by yellow dotted lines in Fig. 5e and f, respectively). At the same time, around the local mixing zones formed in the amorphous ribbon, layers of

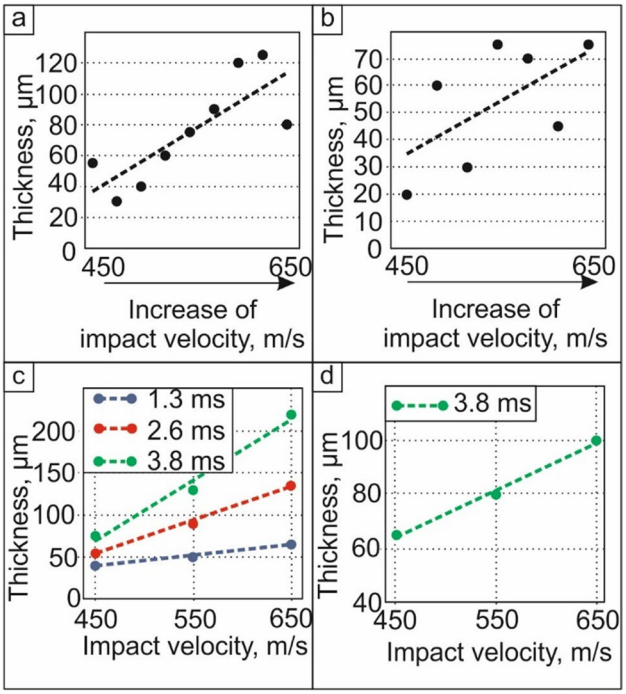

Fig. 6 Thicknesses of the deformed layers in titanium obtained experimentally (**a**, **b**) and from simulation (**c**, **d**). a, c — upper titanium plate; b, d — lower titanium plate. Impact velocities in all figures are given for the upper titanium plate: a, b — experimentally measured, c, d — obtained by numerical simulation

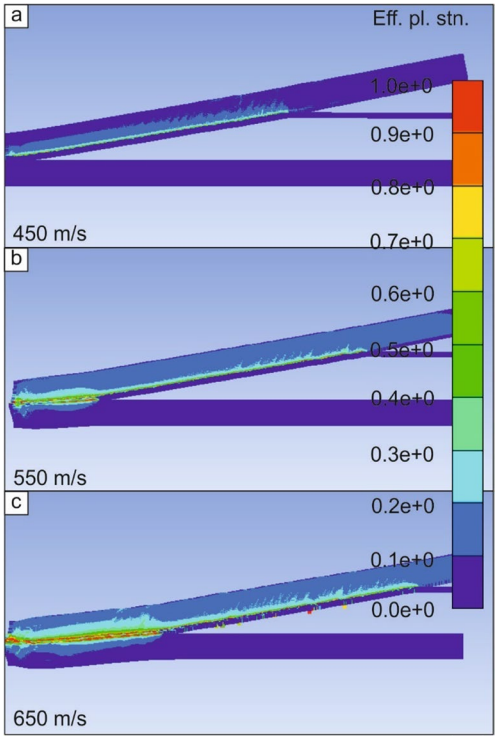

Fig. 7 Effective plastic strain in the materials collided at velocities of 450, 550 and 650 m/s after 2.6 ms after the collision started (simulation results)

recrystallized grains reached a thickness of 15–30 μm. The recrystallization of Ti probably occurred due to the heat of the molten zones in MG layer.

A large number of mixing zones was observed along the welding interfaces. They were thoroughly analyzed by SEM and EDX. At the initial stages of welding, mixing zones formed not continuously (Fig. 8a) and were observed mainly near the interface between titanium and MG. As the velocity increased, the size of the mixing zones also increased, and in areas formed at the highest impact velocities near the end of the joint, mixing was observed throughout the entire thickness of the amorphous ribbon (Fig. 8b, c). In this case, the formation of large mixing zones was accompanied by the formation of pores, which indicate the melting of MG layer. The melting temperature of Zr-based MG is quite low and equal to 712 °C, while the melting temperature of Ti is much higher (1668 °C). For this reason, one can expect that MG will begin to melt before Ti. Under the more severe welding regimes, the melted volumes of MG are expected to be larger. Ti can be mixed with MG being in a solid or liquid state. The latter is possible if the temperature in the impact zone reaches Ti melting point. The temperatures at the interface during collision are discussed below.

From numerical simulation, it follows that with increasing impact velocity, the temperature in the upper weld increased from 660 to 1600 K, and at the lower interface increased from 740 to 4500 K (Fig. 9). The results of materials characterization also evidence that more intense melting occurs with increase of the impact velocity which is a result of higher heating temperature. It can be noticed that the size of the mixing zones at the initial part of the welding interface was smaller than in the final ones. Besides, mixing zones formed at medium collision velocities at the upper and lower interfaces (Fig. 8b) had different structures. The mixing zones adjacent to the upper interface were denser and less saturated with titanium (Fig. 8d). For this reason, one can conclude that the results of simulation are in agreement with the experimental data.

Based on the simulation results, one can conclude that deformation of MG occurs through a shear mechanism. In Fig. 10c, one can observe the development of such deformation processes. In turn, intense local deformations cause heating of the corresponding zones resulting in the formation of locally melted and mixed areas. It is obvious that some part of MG ribbons had temperatures corresponding to the supercooled liquid state. It is known that near the glass transition temperature range, MGs transform into a superplastic state [43]. This can be a factor which improves the weldability of amorphous ribbons during high-velocity impact welding.

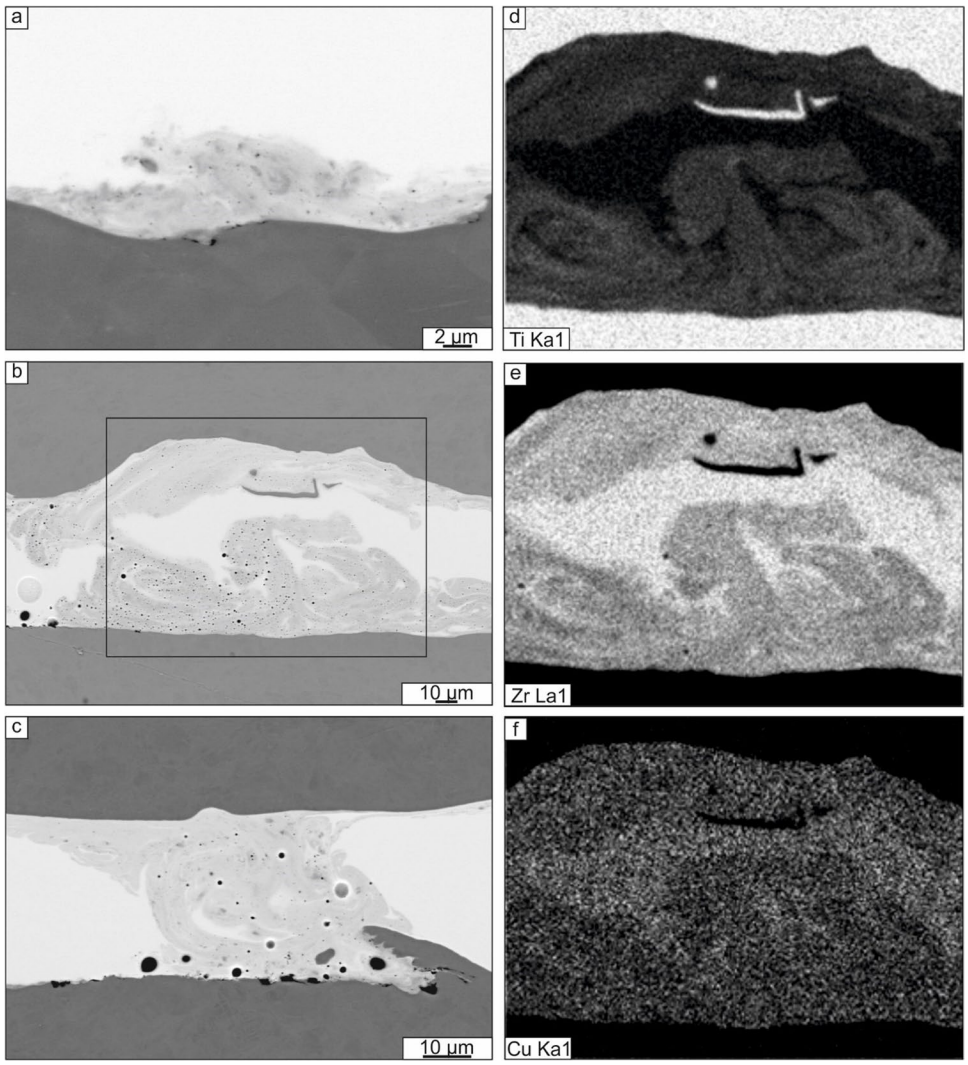

Fig. 8 Mixing zones formed in the MG layer (**a**–**c**) and elemental mapping of the zone shown in b (**d**–**f**). From a to c the impact velocity increased from 450 to 650 m/s

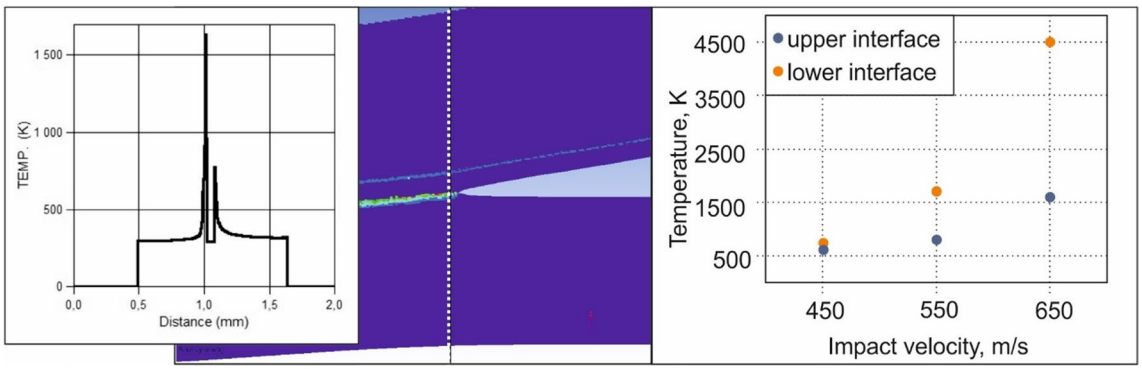

Fig. 9 Temperatures near the contact point at the lower and upper interfaces as a function of the collision velocity. Results correspond to 1.3 ms after the collision started for the upper interface and to 3.8 ms for the lower interface

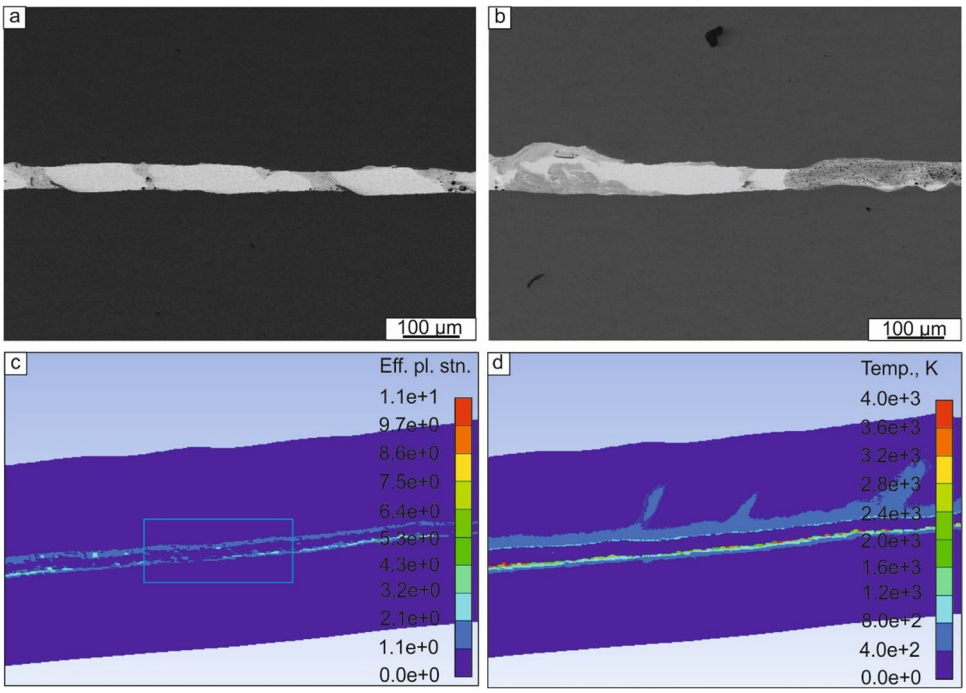

Fig. 10 Location of the mixing zones formed in metallic glass (**a**, **b**) and distribution of strains and temperatures in the materials subjected to oblique impact (**c**, **d**). a, b — SEM images; c, d — results of simulation

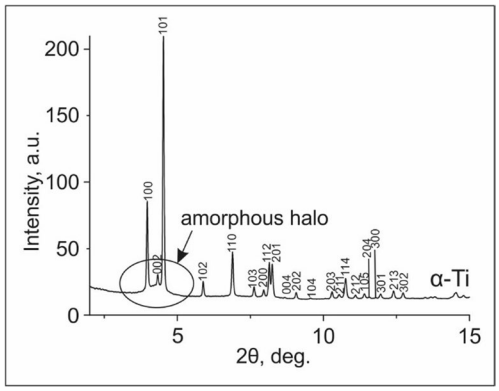

Fig. 11 SXRD pattern obtained from the composite in transmission mode

It should be noted that all of the abovementioned mixing zones are arranged locally. If the local formation of mixing zones that result from the shear bands is natural, the formation of separate mixing zones in other areas (as, for example, in Fig. 10b) may be associated with uneven temperature distribution along the weld (Fig. 10d).

XRD analysis revealed that, despite the development of melting processes in separate zones of MG, its crystallization did not occur (Fig. 11). The XRD pattern shows only peaks corresponding to α-Ti, as well as halo in 2θ range from approximately 3.5 to 5°. The presence of halo indicates a disordered phase in the structure of the composite.

3.2 Mechanical properties of the composite

The mechanical properties of the composite were assessed by tensile tests and nanoindentation. It is known that impact welding is accompanied by strain hardening of the materials [44]. For example, the strength of explosively welded cp-Ti plates increased by 20% compared to the initial state [45]. Structural studies of the Ti-MG-Ti composite obtained in this study also indicate that during MPW, the material experiences severe plastic deformation. It is reasonable to assume that MPW should also be accompanied by strain hardening which is clearly seen from nanoindentation in a titanium layer (Fig. 12). Strain hardening of interfacial regions is a characteristic of both Ti layers. As LM analysis has shown (Figs. 5 and 6), both interfaces were subjected to plastic strain, however, the thickness of the deformed zone was higher for the upper Ti plate. For this reason, the thickness of the hardened layer is expected to be different.

When measuring tensile strength of the composite, it is important to separate the effect of strengthening due to the MG layer and the effect of strain hardening due to impact of the plates. For this reason, the Ti–Ti bimetal obtained in the same way as the Ti-MG-Ti composite was used as a reference material. Tensile strength of bimetallic sample was close to 500 MPa (Fig. 13).

When a stronger phase is added to a material, an increase in its strength can be estimated using the rule of mixtures [46]:

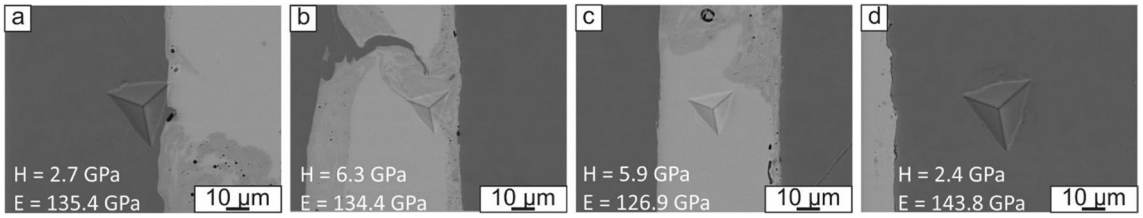

Fig. 12 Nanohardness and elastic properties of the composite at: **a** — titanium near the interface with MG; **b** — mixing zone; **c** — MG layer, **d** — Ti layer

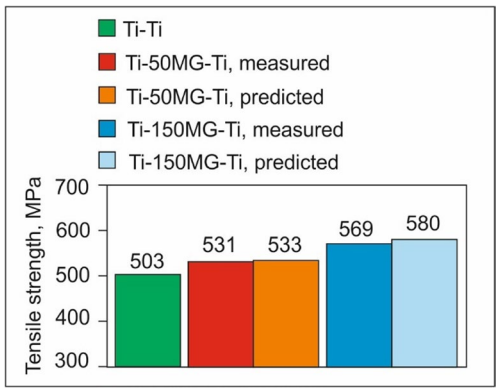

Fig. 13 Ultimate tensile strength of the composites reinforced by 0–13 vol. % of MG

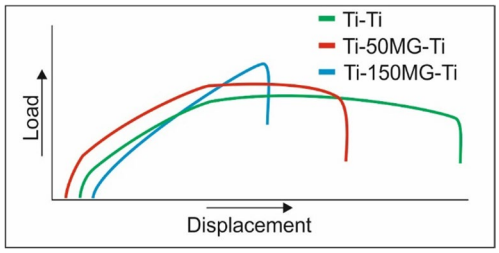

Fig. 14 Typical load–displacement curves obtained when testing composites under uniaxial tension conditions

$$\sigma_c = \sigma_{Ti} V_{fTi} + \sigma_{MG} V_{fMG}$$

,

Where σ_{MG} = 1120 MPa (ultimate tensile strength of Zr-based MG ribbon) and σ_{Ti} = 503 MPa (ultimate tensile strength of Ti–Ti bimetal). V_{fMG} and V_{fTi} are the volume fractions of MG ribbon and Ti in the composite. With the thickness of MG ribbons equal to 50 μm and 150 μm, its volume fraction in the sample was 5% and 13%, respectively. Therefore, the predicted value of ultimate tensile strength at volume fractions of 5% and 13% is 533 and 580 MPa, respectively. The experimental values obtained by testing the composites with 50 μm and 150 μm MG layers were 531 and 569 MPa, respectively, which is in good agreement with the calculated values.

No steps corresponding to a drop in load were observed in the load–displacement curves, which indicates that the materials were deformed uniformly, without delamination along the interphase boundaries (Fig. 14). This character of the curves also indicates the simultaneous destruction of titanium and amorphous alloy. The results obtained evidence the effectiveness of combining titanium and MG.

4 Discussion

4.1 Particularities of impact welding of titanium and MG

High-velocity impact welding is a rapidly proceeding process in which the interaction of the materials lasts a fraction of a second. Deformation, heating, and cooling occur at high rates and are localized mainly near the interface, which allows the amorphous structure of MG to be preserved. The strains and temperatures achieved in these surface layers are very high and depend directly on the impact conditions. Experimental studies and numerical simulation have shown that an increase in impact velocity leads to an increase in the deformation of the material adjacent to the impact zone. A greater energy input that occurs with increasing impact velocity leads to a more intense development of deformation processes (Fig. 7).

Deformation is an important factor contributing to the formation of a weld joint. In addition to the fact that intense deformation provides so called “self-cleaning” effects, it also promotes activation of surfaces, which is related to the number of dislocations terminating on the surfaces of the plates [47]. According to [48], a 0.5–0.9 plastic strain is sufficient for materials to be welded. According to the experimental data obtained, this plastic strain was achieved already at the initial stages of welding (at an impact velocity of 450 m/s) which is evidenced by the formation of reliable joint without any defects. A further increase in velocity led to excessive deformation resulting in a number of effects observed in microstructural images (Figs. 5 and 8). Plastic work leads

to heat generation. Due to short duration of processes occurring during impact welding, the heat does not have enough time to be evenly distributed, but is concentrated in local areas, which leads to the appearance of remelting zones. In addition, local heating can be facilitated by friction between jet with the surfaces of the plates [49].

Due to the much lower melting temperature of Zr-based ribbon, the remelting zones were concentrated predominantly in this layer. It was shown in study [39] that resolidification of Zr-based alloy can already be achieved at loading speed of 415 m/s. The transfer of heat from these zones into the surrounding material promotes its local melting and subsequent solidification, which can be clearly seen in Fig. 5a, c, d. Titanium adjacent to the mixing areas was characterized by the formation of equiaxial grains elongated in the direction of the heat removal. The temperature exceeding the melting point of Ti was achieved at the interface at a collision velocity above 550 m/s (Fig. 9). The local melting of titanium near the mixing zones explains their saturation with nitrogen, which was observed in our earlier studies by electron diffraction and SXRD analysis [33, 34]. In the local areas of mixing zones adjoining the boundary with titanium, nanosized inclusions of titanium nitride were found. The formation of these particles explains the slight increase in hardness in these areas (Fig. 12b, c). At the same time, the formation of a fine-grained structure in titanium along the entire interface with MG is a consequence of recrystallization of a highly deformed material. An increase in collision velocity leads to an increase in plastic work, heating, and, as a consequence, to an increase in the thickness of the layer of recrystallized grains (Fig. 5e, f).

The behavior of MG under dynamic loads is significantly different from that of titanium. With rare exceptions, MGs are practically not plastically deformed. Lu et al. [50] found that at high loading rates, plastic flow in bulk metallic glass can develop in micro areas according to the mechanism of random nucleation and growth of microvoids, and the appearance of microplastic flow is possible in the case of thermal softening at a temperature below a glass transition point. In macrovolumes, deformation of MG occurs through the formation of shear bands. The initiation of shear bands can result from early defects formed during casting, and the direction of the shear bands is determined by the stress fields arising during loading [51]. In the case of high-velocity impact welding, shear bands propagate at an angle of 45° to the interface, as has been observed in numerous studies of various explosively welded material couples [49, 52, 53]. Shear deformations developed during dynamic loading cause the release of heat, which cannot be evenly distributed due to the lack of time [49]. This adiabatic phenomenon leads to a local increase in the temperature of the material. Consequently, thermal softening contributes to an increase in plastic strain of these local areas. Temperature and shear stress together cause a collective glide of atoms in glassy alloy and, as a consequence, the formation of wide adiabatic bands that spread throughout the entire thickness of the ribbon (Fig. 10a, c), and a local increase in temperature promotes the melting of the material in these zones. Therefore, local temperature raise induces the melting of these areas.

Despite the absence of other deformation processes in MG, high-velocity impact welding of titanium and Zr-based glassy alloy is nevertheless possible. This is explained by the fact that for welding, it is enough for a softer material to flow over the surface of a harder one; this flow leads to the removal of impurities and activates the surface of the harder plate [48].

The processes described above occurred predominantly near the interfaces or in local shear zones. This allows to preserve the amorphous state of MG during the MPW. Moreover, the mixing zones resulting from melting and interfusion with titanium were subjected to re-amorphization due to rapid heat removal [30, 32].

4.2 Possibilities of further strengthening titanium with MGs

Mechanical tests of the composites showed that the reinforcement effect of MG is proportional to its volume fraction. When 5% MG was added to titanium, its strength increased by 5%; when the fraction of BMG increased to 13%, the increase in strength reached 13% (Fig. 13). Thus, it can be predicted that an increase in the amorphous phase fraction to 50% can lead to an increase in strength by 50% or even 60%, according to a rule of mixtures. At the same time, fabrication of MG ribbons with a thickness comparable to the thickness of titanium can be a challenging task. For this reason, a higher volume fraction of the glassy phase in the composite can be achieved by reducing the thickness of titanium workpieces. This, however, will result in a reduction of the final thickness of the composite. This problem can be solved by increasing the number of layers to reach the required thickness. When using MPW or EW for fabrication of laminated composites, one must take into account that at each subsequent interface the impact velocity decreases, which can lead to unwelded spots at the lower interfaces. Thus, this approach requires further experimental confirmation. On the other hand, the required thickness can be obtained by welding in several steps which include fabrication of several three-layer workpieces and welding them together to form a nine-layer composite, as was shown in the study [54]. Alternatively, the composition of MG can be changed.

Currently, the literature contains an extensive data collection on the composition and properties of metallic glasses with a wide range of properties [55, 56], and the choice of the appropriate MG composition should be based on the potential application field (engineering, biomedical, etc.).

5 Conclusions

1. A three-layer laminated composites consisted of two titanium plates and Zr-based MG ribbon between them were successfully fabricated by MPW. The quality of both interfaces was high, without defects and unwelded spots. XRD analysis revealed that disordered structure of MG ribbons was preserved.
2. During welding process, the impact velocity increased from 450 to 650 m/s, which resulted in the raise of plastic strain and heating intensity along the interface. Experimental data and simulation results evidence that the second interface was subjected to lower deformation, but higher heating compared to the first one, which is due to the decrease in impact velocity and increase in the flyer mass. MG was mainly subjected to shear deformation with formation of broad shear bands extending through the entire thickness of the ribbons.
3. Localization of the plastic strain induced the excessive heating. This can improve the ductility of MG when the supercooled liquid conditions are reached. The localized plastic flow and heating also result in formation of molten regions which can be saturated with atmospheric gases. When cooling, these zones underwent re-amorphization.
4. Tensile tests revealed that strength of composites increased proportionally to the volume fraction of MG in their structure. Addition of 5 and 13% of Zr-based MG to titanium increased its ultimate tensile strength from 503 to 531 and 569 MPa, respectively.

Acknowledgements Research was conducted at core facility "Structure, mechanical and physical properties of materials" (agreement with the Ministry of Science and Higher Education of the Russian Federation No 13.CKP.21.0034, 075-15-2021-698)

Author contribution D.V. Lazurenko: conceptualization, formal analysis, writing—original draft, investigation, supervision, funding acquisition; A.A. Ivannikov: conceptualization, investigation, data curation, formal analysis, writing—review & editing; A.G. Anisimov: resources, investigation, validation; N.S. Popov: investigation, methodology, visualization; K.I. Emurlaev: investigation, formal analysis; G.D. Dovzhenko: formal analysis, writing—review & editing; I.A. Bataev: formal analysis, writing—review & editing; R.I. Kuzmin: investigation; K.E. Kuper: resources.

Funding The study was financially supported by the Russian Science Foundation Grant No. 22–23-00953, https://rscf.ru/project/22-23-00953/.

Declarations

Competing interests The authors declare no competing interests.

References

1. Schuh CA, Hufnagel TC, Ramamurty U (2007) Mechanical behavior of amorphous alloys. Acta Mater 55:4067–4109. https://doi.org/10.1016/j.actamat.2007.01.052
2. Trexler MM, Thadhani NN (2010) Mechanical properties of bulk metallic glasses. Prog Mater Sci 55:759–839. https://doi.org/10.1016/j.pmatsci.2010.04.002
3. Inoue A (2000) Stabilization of metallic supercooled liquid and bulk amorphous alloys. Acta Mater 48:279–306. https://doi.org/10.1016/S1359-6454(99)00300-6
4. Eckert J, Das J, Pauly S, Duhamel C (2007) Mechanical properties of bulk metallic glasses and composites. J Mater Res 22:285–301. https://doi.org/10.1557/jmr.2007.0050
5. Georgarakis K, Dudina DV, Kvashnin VI (2022) Metallic glass-reinforced metal matrix composites: design, interfaces and properties. Materials 15:8278. https://doi.org/10.3390/ma15238278
6. Cytron SJ (1982) A metallic glass-metal matrix composite. J Mater Sci Lett 1:211–213. https://doi.org/10.1007/BF00724898
7. Lee MH, Kim JH, Park JS, Kim JC, Kim WT, Kim DH (2004) Fabrication of Ni–Nb–Ta metallic glass reinforced Al-based alloy matrix composites by infiltration casting process. Scripta Mater 50:1367–1371. https://doi.org/10.1016/j.scriptamat.2004.02.038
8. Lee MH, Park JS, Kim JH, Kim WT, Kim DH (2005) Synthesis of bulk amorphous alloy and composites by warm rolling process. Mater Lett 59:1042–1045. https://doi.org/10.1016/j.matlet.2004.10.078
9. Mathaudhu SN, Ted Hartwig K, Karaman I (2007) Consolidation of blended powders by severe plastic deformation to form amorphous metal matrix composites. J Non-Cryst Solids 353:185–193. https://doi.org/10.1016/j.jnoncrysol.2006.06.009
10. Bao W, Chen J, Yang X, Xiang T, Cai Z, Xie G (2022) Improved strength and conductivity of metallic-glass-reinforced nanocrystalline CuCrZr alloy. Mater Design 214:110420. https://doi.org/10.1016/j.matdes.2022.110420
11. Wang Z, Georgarakis K, Nakayama KS, Li Y, Tsarkov AA, Xie G, Dudina D, Louzguine-Luzgin DV, Yavari AR (2016) Microstructure and mechanical behavior of metallic glass fiber-reinforced Al alloy matrix composites. Sci Rep-UK 6:24384. https://doi.org/10.1038/srep24384
12. Yu P, Kim KB, Das J, Baier F, Xu W, Eckert J (2006) Fabrication and mechanical properties of Ni–Nb metallic glass particle-reinforced Al-based metal matrix composite. Scripta Mater 54:1445–1450. https://doi.org/10.1016/j.scriptamat.2006.01.001
13. Aljerf M, Georgarakis K, Louzguine-Luzgin D, Le Moulec A, Inoue A, Yavari AR (2012) Strong and light metal matrix composites with metallic glass particulate reinforcement. Mat Sci Eng A-Struct 532:325–330. https://doi.org/10.1016/j.msea.2011.10.098
14. Wang Z, Tan J, Sun BA, Scudino S, Prashanth KG, Zhang WW, Li YY, Eckert J (2014) Fabrication and mechanical properties of Al-based metal matrix composites reinforced with Mg65Cu20Zn5Y10 metallic glass particles. Mat Sci Eng A-Srtuct 600:53–58. https://doi.org/10.1016/j.msea.2014.02.003

15. Yu P, Venkataraman S, Das J, Zhang L, Zhang W, Eckert J (2007) Effect of high pressure during the fabrication on the thermal and mechanical properties of amorphous Ni60Nb40 particle-reinforced Al-based metal matrix composites. J Mater Res 22:1168–1173. https://doi.org/10.1557/jmr.2007.0158
16. Kvashnin VI, Dudina DV, Ukhina AV, Koga GY, Georgarakis K (2022) The benefit of the glassy state of reinforcing particles for the densification of aluminum matrix composites. J Compos Sci 6:135. https://doi.org/10.3390/jcs6050135
17. Perrière L, Champion Y (2012) Phases distribution dependent strength in metallic glass–aluminium composites prepared by spark plasma sintering. Mat Sci Eng A-Struct 548:112–117. https://doi.org/10.1016/j.msea.2012.03.100
18. Bao W, Chen J, Xie G (2022) Optimized strength and conductivity of multi-scale copper alloy/metallic glass composites tuned by a one-step spark plasma sintering (SPS) process. J Mater Sci Technol 128:22–30. https://doi.org/10.1016/j.jmst.2022.04.024
19. Scudino S, Surreddi KB, Sager S, Sakaliyska M, Kim JS, Löser W, Eckert J (2008) Production and mechanical properties of metallic glass-reinforced Al-based metal matrix composites. J Mater Sci 40:4518–4526. https://doi.org/10.1007/s10853-008-2647-5
20. Kalyankar V, Bhoskar A, Deshmukh D, Patil S (2022) On the performance of metallurgical behaviour of Stellite 6 cladding deposited on SS316L substrate with PTAW process. Can Metall Quart 61:130–144. https://doi.org/10.1080/00084433.2022.2031681
21. Bhoskar A, Kalyankar V, Deshmukh D (2023) Metallurgical characterisation of multi-track Stellite 6 coating on SS316L substrate. Can Metall Quar 62:665–677. https://doi.org/10.1080/00084433.2022.2149009
22. Santana DA, Koga GY, Wolf W, Bataev IA, Ruktuev AA, Bolfarini C, Kiminami CS, Botta WJ, Jorge AM Jr (2020) Wear-resistant boride reinforced steel coatings produced by non-vacuum electron beam cladding. Surf Coat Tech 386:125466. https://doi.org/10.1016/j.surfcoat.2020.125466
23. Lee K, Yun E, Lee S, Kim NJ (2005) Fabrication of Zr- and Cu-base bulk metallic glass/Cu surface composites by high-energy electron-beam irradiation. Mat Sci Eng A-Srtuct 408:92–101. https://doi.org/10.1016/j.msea.2005.07.044
24 Ibrahim MZ, Sarhan AAD, Shaikh MO, Kuo TY, Yusuf F, Hamdi M (2018) Investigate the effects of the laser cladding parameters on the microstructure, phases formation, mechanical and corrosion properties of metallic glasses coatings for biomedical implant application. In: AlMangour B (ed) Additive Manufacturing of Emerging Materials. Springer, Cham, pp 299–323. https://doi.org/10.1007/978-3-319-91713-9_10
25. Sohrabi N, Panikar RS, Jhabvala J, Buch AR, Mischler S, Logé RE (2020) Laser coating of a Zr-based metallic glass on an aluminum substrate. Surf Coat Tech 400:126223. https://doi.org/10.1016/j.surfcoat.2020.126223
26. Liu KX, Liu WD, Wang JT, Yan HH, Li XJ, Huang YJ, Wei XS, Shen J (2008) Atomic-scale bonding of bulk metallic glass to crystalline aluminum. Appl Phys Lett 93:081918. https://doi.org/10.1063/1.2976667
27. Hanliang L, Ning L, Xiaojie L, Xin S, Tao S, Zhanguo M (2019) Joining of Zr60Ti17Cu12Ni11 bulk metallic glass and aluminum 1060 by underwater explosive welding method. J Manuf Process 45:115–122. https://doi.org/10.1016/j.jmapro.2019.06.035
28. Liang H, Luo N, Shen T, Sun X, Fan X, Cao Y (2020) Experimental and numerical simulation study of Zr-based BMG/Al composites manufactured by underwater explosive welding. J Mater Res Tech 9:1539–1548. https://doi.org/10.1016/j.jmrt.2019.11.079
29. Hokamoto K, Nakata K, Mori A, Ii S, Tomoshige R, Tsuda S, Tsumura T, Inoue A (2009) Microstructural characterization of explosively welded rapidly solidified foil and stainless steel plate through the acceleration employing underwater shock wave. J Alloy Compd 485:817–821. https://doi.org/10.1016/j.jallcom.2009.06.082
30. Hokamoto K, Nakata K, Mori A, Tsuda S, Tsumura T, Inoue A (2009) Dissimilar material welding of rapidly solidified foil and stainless steel plate using underwater explosive welding technique. J Alloy Compd 472:507–511. https://doi.org/10.1016/j.jallcom.2008.05.002
31. Feng J, Chen P, Zhou Q (2018) Investigation on explosive welding of Zr53Cu35Al12 bulk metallic glass with crystalline copper. J Mater Eng Perform 27:2932–2937. https://doi.org/10.1007/s11665-018-3396-5
32. Bataev IA, Lazurenko DV, Tanaka S, Hokamoto K, Bataev AA, Guo Y, Jorge AM Jr (2017) High cooling rates and metastable phases at the interfaces of explosively welded materials. Acta Mater 135:277–289. https://doi.org/10.1016/j.actamat.2017.06.038
33. Lazurenko DV, Anisimov AG, Popov NS, Dovzhenko GD, Bataev IA, Emurlaev KI, Ogneva TS, Golovin ED (2022) Joining Ti-based metallic glass and crystalline titanium by magnetic pulse welding. J Non-Cryst Solids 597:121912. https://doi.org/10.1016/j.jnoncrysol.2022.121912
34. Lazurenko DV, Ivannikov AA, Anisimov AG, Popov NS, Dovzhenko GD (2023) Formation of composite material by magnetic pulse welding of crystalline titanium and nickel-base amorphous alloy. Met Sci Heat Treat 815:47–54. https://doi.org/10.1007/s11041-023-00931-0
35. Kalin BA, Fedotov VT, Sevryukov ON, Grigor'ev AE (1996) Amorphous strip brazing alloys for high-temperature brazing. Experience with developing production technology and application. Weld Int 10:578–581. https://doi.org/10.1080/09507119609549053
36. Anisimov AG, Mali VI (2018) Specific features of sheet acceleration under conditions of magnetic pulse welding. Combust Explos Shock Waves 54:113–118. https://doi.org/10.1134/S0010508218010161
37. Kieffer J, Wright JP (2013) PyFAI: a Python library for high performance azimuthal integration on GPU. Powder Diffr 28:S339–S350. https://doi.org/10.1017/S0885715613000924
38. Nassiri A, Zhang S, Lee T, Abke T, Vivek A, Kinsey B, Daehn G (2017) Numerical investigation of CP-Ti & Cu110 impact welding using smoothed particle hydrodynamics and arbitrary Lagrangian-Eulerian methods. J Manuf Process 28:558–564. https://doi.org/10.1016/j.jmapro.2017.04.032
39. Tan Y, Wang YW, An R, Fu Q, Xu ZQ, Cheng XW, Cheng HW (2021) Dynamic mechanical performance and constitutive model for Zr58Cu12Ni12Al15Nb3 metallic glass. J Mater Res Technol 13:1866–1877. https://doi.org/10.1016/j.jmrt.2021.05.087
40. Hokamoto K, Chiba A, Fujita M, Izuma T (1995) Single-shot explosive welding technique for the fabrication of multilayered metal base composites: effect of welding parameters leading to optimum bonding condition. Comp Eng 5:1069–1079. https://doi.org/10.1016/0961-9526(95)00059-V
41. Wang WH, Dong C, Shek CH (2004) Bulk metallic glasses. Mat Sci Eng R 44:45–89. https://doi.org/10.1016/j.mser.2004.03.001
42. Wang WH (2012) The elastic properties, elastic models and elastic perspectives of metallic glasses. Prog Mater Sci 57:487–656. https://doi.org/10.1016/j.pmatsci.2011.07.001
43. Nieh TG, Mukai T, Liu CT, Wadsworth J (1999) Superplastic behavior of a Zr–10Al–5Ti-–17.9Cu–14.6Ni metallic glass in the supercooled liquid region. Scripta Mater 40:1021–1027. https://doi.org/10.1016/S1359-6462(99)00071-8
44. Bataev I, Bataev A, Mali V, Esikov M, V. B, (2011) Peculiarities of weld seams and adjacent zones structures formed in process of explosive welding of sheet steel plates. Mater Sci Forum 673:95–100. https://doi.org/10.4028/www.scientific.net/MSF.673.95

45. Makarova EB, Esikov MA, Gontarenko AS, Sameishcheva TS (2012) Structural changes in VT1–0 titanium induced by deformation during explosion welding. Russian Metall 2012:826–830. https://doi.org/10.1134/S0036029512090054
46. Agarwal BD, Broutman LJ, Chandrashekhara K (2017) Analysis and performance of fiber composites. John Wiley & Sons, UK
47. Karakozov ES (1976) Soedinenie metallov v tverdoy faze. Metallurgia, Moscow [in Russian]
48. Zakharenko ID (1990) Svarka metallov vzryvom (Explosive welding of metals). Nauka i tehnika, Minsk, p 205 [in Russian]
49. ZareieRajani HR, Akbari Mousavi SAA (2012) The effect of explosive welding parameters on metallurgical and mechanical interfacial features of Inconel 625/plain carbon steel bimetal plate. Mater Sci Eng A-Struct 556:454–464. https://doi.org/10.1016/j.msea.2012.07.012
50. Lu L, Li C, Wang WH, Zhu MH, Gong XL, Luo SN (2016) Ductile fracture of bulk metallic glass Zr50Cu40Al10 under high strain-rate loading. Mater Sci Eng A-Struct 651:848–853. https://doi.org/10.1016/j.msea.2015.11.040
51. Mo Y, Meng L, Yao X (2022) The formation and propagation mechanism of shear band in bulk metallic glasses under dynamic compression. Mater Sci Eng A-Struct 844:143165. https://doi.org/10.1016/j.msea.2022.143165
52. Song J, Kostka A, Veehmayer M, Raabe D (2011) Hierarchical microstructure of explosive joints: example of titanium to steel cladding. Mater Sci Eng A-Struct 528:2641–2647. https://doi.org/10.1016/j.msea.2010.11.092
53. Lazurenko DV, Bataev I, Maliutina I, Kuz'min R, Mali V, Esikov M, Kornienko E, (2018) On the structure and mechanical properties of multilayered composite, obtained by explosive welding of high-strength titanium alloys. J Comp Sci 2:39. https://doi.org/10.3390/jcs2030039
54. Bataev I, Bataev A, Mali V, Burov V, Golovin E, Smirnov A, Prikhodko E (2011) Structure and fatigue crack resistance of multilayer materials produced by explosive welding. Adv Mat Res 287–290:108–111. https://doi.org/10.4028/www.scientific.net/AMR.287-290.108
55. Khan MM, Nemati A, Rahman ZU, Shah UH, Asgar H, Haider W (2018) Recent advancements in bulk metallic glasses and their applications: a review. Crc Cr Rev Sol State 43:233–268. https://doi.org/10.1080/10408436.2017.1358149
56. Kruzic JJ (2016) Bulk metallic glasses as structural materials: a review. Adv Eng Mater 18:1308–1331. https://doi.org/10.1002/adem.201600066